

High-resolution Image Registration of Consecutive and Re-stained Sections in Histopathology

Johannes Lotz, Nick Weiss, Jeroen van der Laak, and Stefan Heldmann

Abstract— We compare variational image registration in consecutive and re-stained sections from histopathology. We present a fully-automatic algorithm for non-parametric (nonlinear) image registration and apply it to a previously existing dataset from the ANHIR challenge (230 slide pairs, consecutive sections) and a new dataset (hybrid re-stained and consecutive, 81 slide pairs, ca. 3000 landmarks) which is made publicly available. Registration hyperparameters are obtained in the ANHIR dataset and applied to the new dataset without modification. In the new dataset, landmark errors after registration range from 13.2 μm for consecutive sections to 1 μm for re-stained sections. We observe that non-parametric registration leads to lower landmark errors in both cases, even though the effect is smaller in re-stained sections. The nucleus-level alignment after non-parametric registration of re-stained sections provides a valuable tool to generate automatic ground-truth for machine learning applications in histopathology.

Index Terms— computational pathology, image registration, histopathology, multiplexing, machine learning

I. INTRODUCTION

In histopathology, much insight into disease subtyping, biomarker discovery, and tissue organization is gained by analyzing differently stained histological sections. For this procedure, a fixed tissue is transferred in a paraffin block and cut into 2-5 μm thin slices. Then, slices are subsequently stained by e.g. immunohistochemistry, and—in a digital workflow—scanned to obtain a digital whole slide image (WSI)[18]. The resulting image can be used for digital analysis, e.g. in biomarker discovery by combining two or more different stains [12]. Other applications include the creation of training sets for deep learning methods in histopathology, as described in [6, 24].

Enabled by digital slide scanners, a re-staining approach which was initially used in fluorescence microscopy and known as tissue-based cyclic immunofluorescence (t-CyCIF) [9, 15] is gaining popularity in brightfield imaging [20, 6, 2]. Instead of staining consecutive sections and scanning them

submitted on: 24.06.2021

Johannes Lotz and Nick Weiss contributed equally.

Johannes Lotz, Nick Weiss and Stefan Heldmann are with the Fraunhofer Institute for Digital Medicine MEVIS, Lübeck, Germany (e-mail: {johannes.lotz, nick.weiss, stefan.heldmann}@mevis.fraunhofer.de)

Jeroen van der Laak is with the Radboud University Medical Center, Nijmegen, The Netherlands (e-mail: Jeroen.vanderLaak@radboudumc.nl).

later, a section is stained and scanned first. In a second step, the stain is washed or bleached and another stain is applied. After re-scanning, both images contain the same tissue with different staining, so that it is possible to compare the same cell with respect to different antibodies or markers. However, we still observe nonlinear deformations in the tissue, which are most likely due to the chemical reactions during the re-staining process.

To recombine the information from each staining, accurate multi-stain image registration is needed. As we show in this work, image registration is required in both, consecutive as well as re-stained, image pairs. In the case of registration of re-stained sections, accuracy is achieved at the nucleus level. In the case of consecutive sections, this level of accuracy cannot usually be reached due to the lack of corresponding objects at the appropriate resolution caused by the slice thickness or distance. Here, a very good registration of structures with a size above the nucleus level can be achieved on the basis of images with relatively low resolution and the use of a nonlinear deformation model.

Below, we first describe the registration method and its application to consecutive slide images in the “automatic nonlinear histological image registration challenge” (ANHIR, anhir.grand-challenge.org), where we determine optimal hyperparameters. We then evaluate the same parameterization on a new publicly available dataset [14] that contains both consecutive and re-stained slides.

II. FULLY-AUTOMATIC IMAGE REGISTRATION

In the following, we present a 3-step registration pipeline that was ranked first in the ANHIR challenge where image registration methods have been evaluated on consecutive images. A quantitative comparison of state-of-the-art image registration methods applied to histopathology images can be found in the challenge results in [5].

The registration pipeline consists of 1) a robust pre-alignment, 2) a parametric registration computed on coarse resolution images, and 3) an accurate nonlinear registration. We base our method on the variational image registration framework first described by Fischer and Modersitzki [8, 17] which has been applied to many clinical fields from histology [22] to radiology [21, 13].

Given a so-called reference image $R : \mathbb{R}^2 \rightarrow \mathbb{R}$ and a so-called template image $T : \mathbb{R}^2 \rightarrow \mathbb{R}$, the goal of image

registration is to find a reasonable spatial transformation $y : \mathbb{R}^2 \rightarrow \mathbb{R}^2$ such that $R(\mathbf{x}) \approx T(y(\mathbf{x}))$, i.e., R and the deformed template $T \circ y$ are similar in an adequate sense.

Following [17], we formulate image registration as the optimization problem $J(R, T, y) \xrightarrow{y} \min$ of an appropriate objective function J with respect to the desired spatial transformation. Key component of the objective function is a so-called distance or image similarity measure that quantifies the quality of the alignment. We use the Normalized Gradient Fields (NGF) distance measure [10] as it has been shown to be robust to different stains and is suitable for multimodal image registration of histological images [6]. For the discretization, 2D images with extents n_1 -by- n_2 are assumed, correspondingly consisting of $N = n_1 \cdot n_2$ pixels with uniform size h in each dimension and pixel centers $\mathbf{x}_1, \dots, \mathbf{x}_N$. The NGF distance measure is given by

$$\text{NGF}(R, T, y) := \frac{h^2}{2} \cdot \sum_{i=1}^N 1 - \left(\frac{\langle \nabla T(y(\mathbf{x}_i)), \nabla R(\mathbf{x}_i) \rangle_\varepsilon}{\|\nabla T(y(\mathbf{x}_i))\|_\varepsilon \|\nabla R(\mathbf{x}_i)\|_\varepsilon} \right)^2$$

with $\langle \mathbf{x}, \mathbf{y} \rangle_\varepsilon = \mathbf{x}^\top \mathbf{y} + \varepsilon^2$, $\|\mathbf{x}\|_\varepsilon := \sqrt{\langle \mathbf{x}, \mathbf{x} \rangle_\varepsilon}$, and the edge parameter ε , which controls the sensitivity to edges in contrast to noise. The NGF distance measure becomes minimal if intensity gradients and edges, respectively, are aligned and which therefore leads to the alignment of morphological structures.

The NGF distance measure is used in all three steps of the registration pipeline: Pre-alignment, parametric registration, and non-parametric (non-linear) registration. In addition, we use a multilevel optimization scheme that starts with the registration of images at low resolution levels and then refines the transformation to higher image resolutions to reduce the risk of converging too early to local minima and to speed up the optimization process [11]. The per-level optimization is performed using a Gauss-Newton type (parametric registration) and L-BFGS quasi-Newton (non-parametric registration) method, see e.g. [17] or [23, 19] for a more detailed discussion and additional strategies.

All of the three following registration steps rely on the edge parameter ε , the number of levels N_{level} of the image pyramid, and the image resolution of finest level. The parameters are set independently for each step and such that the registration error is minimal and the deformation grid is regular in the sense that it is not folded in the image domain. These parameters are shown in Table I.

A. Step 1: Automatic Rotation Alignment (ARA)

Before histological images are recorded, the tissue is cut, preprocessed and stained in a pathology lab.

After this manual process, neighboring tissue slices can end up in arbitrary positions on the object slide (such as upside down or turned in various ways). In general, no assumptions can be made on the initial tissue positioning and—in a first step—we aim to find a rigid alignment, correcting for global translation and global rotation.

Before registration, all images are converted into a multi-level image data format based on sqlite¹ to reduce the time to load the image data². In addition, all images are converted from color to gray scale and inverted to obtain a black background while loading from disk.

Automatic Rotation Alignment (ARA) first determines the center of mass [3] of both images, using the gray values of the pixels as the weights. Let (t_1, t_2) be the vector pointing from the center of mass of the reference image to the center of mass of the template image, and let $\phi_k = 2\pi(k-1)/(N_{\text{rot}}-1)$, $k = 1, \dots, N_{\text{rot}}$ be equidistant rotation angles sampling the interval $[0, 2\pi]$. We then perform N_{rot} rigid registrations starting with the initial guesses (ϕ_k, t_1, t_2) , $k = 1, \dots, N_{\text{rot}}$. Among all N_{rot} rigid registration results, we then select the minimizer with the smallest function value and image distance. Let (ϕ^*, t_1^*, t_2^*) be this minimizer. Then the resulting transformation of the automatic rotation alignment step 1 is defined as

$$y^{\text{ARA}}(\mathbf{x}) := \begin{pmatrix} \cos(\phi^*) & -\sin(\phi^*) \\ \sin(\phi^*) & \cos(\phi^*) \end{pmatrix} \mathbf{x} + \begin{pmatrix} t_1^* \\ t_2^* \end{pmatrix}.$$

B. Step 2: Parametric Registration

The second step of the registration pipeline is a parametric registration with a full affine deformation model. In 2D, an affine deformation y has 6 degrees of freedom and we set

$$y(\mathbf{x}) = \begin{pmatrix} a_1 & a_2 \\ a_4 & a_5 \end{pmatrix} \mathbf{x} + \begin{pmatrix} a_3 \\ a_6 \end{pmatrix}$$

with parameters $a_1, \dots, a_6 \in \mathbb{R}$. We use the rigid transformation y^{ARA} from previous pre-alignment step 1 as initial guess. That is, we setup the initial affine parameters a_1, \dots, a_6 such that

$$\begin{pmatrix} a_1 & a_2 \\ a_4 & a_5 \end{pmatrix} = \begin{pmatrix} \cos(\phi^*) & -\sin(\phi^*) \\ \sin(\phi^*) & \cos(\phi^*) \end{pmatrix} \quad \text{and} \quad \begin{pmatrix} a_3 \\ a_6 \end{pmatrix} = \begin{pmatrix} t_1^* \\ t_2^* \end{pmatrix}.$$

We then minimize the objective function

$$J(R, T, y) = \text{NGF}(R, T, y) \rightarrow \min$$

with respect to the parameters a_1, \dots, a_6 . The resulting transformation is then used as initial guess for a subsequent non-parametric registration.

C. Step 3: Non-parametric Registration

The final step is a non-parametric image registration. Here, the transformation y is given by

$$y(\mathbf{x}) = \mathbf{x} + u(\mathbf{x})$$

with so-called displacement $u : \mathbb{R}^2 \rightarrow \mathbb{R}^2$, $u = (u_1, u_2)$ [17].

In contrast to parametric registration, here the deformation is not restricted to a particular parameterizable deformation model and the nonlinear transformation is controlled by introducing a regularization term into the objective function that measures the deformation energy and penalizes unwanted transformations. Here we use the so-called curvature regularization, which penalizes second-order derivatives of the

¹<https://www.sqlite.org>

²Without image conversion, the image loading time is increased by about five seconds per registration.

displacement [7] and which has been shown to work very well in combination with the NGF distance measure [21, 13]. As with the NGF distance, we evaluate the displacements in the pixel centers $\mathbf{x}_1, \dots, \mathbf{x}_N$ with uniform grid spacing h and use finite differences to approximate the derivatives. Thus, the discretized curvature regularizer is defined as

$$\text{CURV}(y) = \frac{h^2}{2} \sum_{i=1}^N |\Delta^h u_1(\mathbf{x}_i)|^2 + |\Delta^h u_2(\mathbf{x}_i)|^2$$

where Δ^h is the common 5-point finite difference approximation of the 2D Laplacian $\Delta = \partial_{xx} + \partial_{yy}$ with Neumann boundary conditions. In summary, for non-parametric registration, we minimize the objective function

$$J(R, T, y) := \text{NGF}(R, T, y) + \alpha \text{CURV}(y) \rightarrow \min,$$

with respect to the deformation y . The parameter $\alpha > 0$, is a regularization parameter that controls the smoothness of the computed deformation. The regularization parameter α is chosen manually to achieve a smooth deformation and avoid topological changes (lattice folds), while being flexible enough to correct for local changes that improve image similarity. The search space for the displacements u is approximated with 1st order B-splines defined on a uniform control point grid with m points. The resolution of the control point grid is independent of the image resolution and is typically chosen to be much coarser than the image resolution (see also Table I). Finally, we minimize the objective function with respect to the $2m$ B-spline coefficients. For this purpose, we use an L-BFGS quasi-Newton optimization, again with multilevel continuation.

III. APPLICATION TO TWO DATASETS FROM HISTOPATHOLOGY

The algorithm is evaluated on two datasets: The training part of the ANHIR³ challenge data [4] and a previously unpublished dataset, HyReCo [14], that combines re-stained and consecutive sections from histopathology.

A. Evaluation

Following the evaluation in the ANHIR challenge [4], we measure the registration performance as the median (MMrTRE) of the median relative target registration error (MrTRE) over all image pairs $k = 1, \dots, N_{\text{pairs}}$. Since the pixel dimensions are not uniformly available in the ANHIR data, errors are measured relative to the diagonal image size $\sqrt{n_1^2 + n_2^2}$ with n_1, n_2 is the image extent in pixels. The MrTRE over all landmarks of image pair k is computed as

$$\text{MrTRE}_k :=$$

$$\text{median} \left(\left\{ \frac{\|\mathbf{x}_\ell^T - \mathbf{x}_\ell^W\|_2}{\sqrt{n_1^2 + n_2^2}}, \ell = 1, \dots, N_{\text{landmarks}} \right\} \right)$$

where \mathbf{x}_ℓ^T is the ℓ -th template landmark, \mathbf{x}_ℓ^W is the corresponding warped reference landmark, and $N_{\text{landmarks}}$ is the total number of available landmarks in the k -th image pair. Note

that here and in the following, to simplify notation, we refrain from indexing image pair-related symbols, such as landmarks $\mathbf{x}_\ell^T, \mathbf{x}_\ell^W$ or image dimensions n_1, n_2 , according to the image pair number k , since the meaning is clear from the context. However, finally we collect all MrTREs from all images pairs and summarize the results by computing the overall median of all MrTREs with the

$$\text{MMrTRE} := \text{median}(\{\text{MrTRE}_k, k = 1, \dots, N_{\text{pairs}}\}).$$

For the HyReCo data, image pixel sizes are available and additional absolute registration errors can be computed. We compute the median target registration error for dataset k as

$$\text{MTRE}_k :=$$

$$\text{median}(\{\|\mathbf{x}_\ell^T - \mathbf{x}_\ell^W\|_2, \ell = 1, \dots, N_{\text{landmarks}}\})$$

and summarize the MTREs of all datasets by the taking the median

$$\text{MMTRE} := \text{median}(\{\text{MTRE}_k, k = 1, \dots, N_{\text{pairs}}\}).$$

All images in this dataset have a size of approximately 100000×220000 pixels, so the normalized error MrTRE can be obtained by dividing by the diagonal of the slide image. Based on the pixel size $h = 2.43 \cdot 10^{-4} \text{ mm px}^{-1}$ and a diagonal $\sqrt{n_1^2 + n_2^2} \cdot 2.45 \cdot 10^5 \text{ px}$, the relative error is computed as $\text{MrTRE} = \text{MTRE} / (h \cdot \sqrt{n_1^2 + n_2^2}) = \text{MTRE} \cdot 1.68 \cdot 10^{-2} \text{ mm}^{-1}$.

B. Results on ANHIR Challenge Data

The public part of the challenge dataset consists of 230 image pairs with 18 different stains.

We apply the 3-step registration pipeline to the complete training dataset. The reduction of the registration error in the training data after each step in the pipeline is shown in the box plots in Figure 1. While the median error is reduced after each step, those cases that fail in the pre-alignment cannot be recovered at a later stage. Figure 2 shows one of the image pairs after pre-alignment, parametric registration, and non-parametric registration.

The resulting deformations do not contain any grid foldings. The average maximum area change in one grid cell was 1.35%.

The algorithm is robust in 99.6% of the training cases ($N_{\text{pairs}} = 230$). Robustness in the ANHIR challenge is defined as the percentage of the cases where the landmark error is reduced compared to the initial positioning prior to registration.

After registration, a landmark error for the public training data ($N_{\text{pairs}} = 230$) of MMrTRE = 0.19% is reached (see [5] for full challenge results).

The whole registration process including image loading, pre-alignment, parametric and non-parametric registration takes on average 4.0 seconds on an Intel(R) Core(TM) i7-7700K CPU (4.20GHz, four cores) with 32 GB of RAM.

Multiple parameterizations were tested on the training data and the parameter set with the lowest median median rTRE (MMrTRE) was selected (Table I). Except of the finest image resolution, the resulting parameterization of the algorithm has

³<https://anhir.grand-challenge.org>

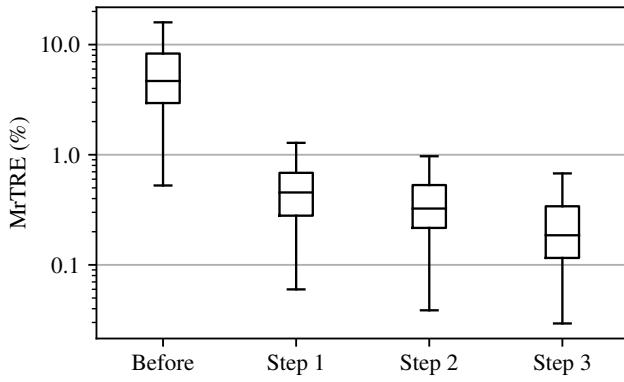


Fig. 1. Median-rTRE measured on the training data ($N_{\text{pairs}} = 230$) before alignment and after each registration step.

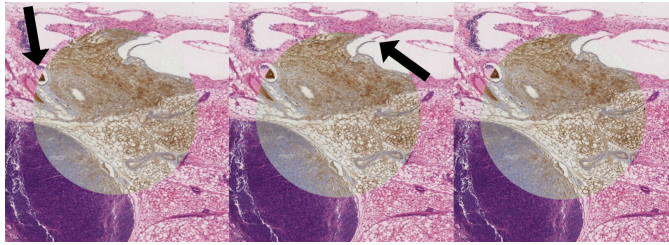


Fig. 2. Spy-view of an image pair after pre-alignment, parametric and non-parametric registration (left to right). Arrows indicate tissue regions with misalignment.

been applied without modifications to the previously unseen HyReCo dataset. The image pyramid was adapted such that the coarsest image resolution matches in both datasets.

C. Results on Hybrid Re-stained and Consecutive Data (HyReCo)

The second dataset was acquired at the Radboud University Medical Center, Nijmegen, the Netherlands⁴. It consists of nine datasets of consecutive sections, each containing four slides stained with H&E, CD8, CD45RO, Ki67, respectively (Figure 3). In addition, PHH3-stained slides have been produced by removing the cover slip from the H&E-stained slide, bleaching the H&E stain, re-staining the same section with PHH3 and scanning it again, similar to the T-CyCIF technique [9, 15] that is well established in fluorescence imaging. For each of these sections, 11–19 landmarks (138 per stain, 690 in total) have been placed manually on corresponding structures and verified by two experienced researchers.

Finding the same points across of several consecutive slides is quite difficult, because care must be taken to locate a similar point in all slides simultaneously. In contrast to these consecutive sections, an image pair of re-stained sections contains the same cells and nuclei such that a one-to-one correspondence can be found for most structures. To overcome the limitations in annotation accuracy imposed by the simultaneous annotation of consecutive and re-stained slides,

⁴The requirement for ethical approval was waived by the IRB of Radboudumc, Nijmegen, the Netherlands, under file number 2020-6972.

TABLE I
PARAMETERS USED IN THE REGISTRATION PIPELINE WHEN APPLIED TO ANHIR CHALLENGE DATA. * INDICATES PARAMETERS THAT DIFFER IN THE HYReCo DATASET.

Step 1: Pre-Alignment

Number of levels N_{level}	4
Number of rotation angles N_{rot}	32
finest image resolution and size	249.1 $\mu\text{m}/\text{px}$, 100×215 px*
NGF ε	0.1

Step 2: Parametric Registration

finest image resolution and size	62.3 $\mu\text{m}/\text{px}$, 390×860 px*
Number of levels N_{level}	5*
NGF ε	0.1

Step 3: Non-Parametric Registration

finest image resolution and size	7.78 $\mu\text{m}/\text{px}$, 3120×6880 px*
number of levels N_{level}	7*
NGF ε	1.0
regularizer parameter α	0.1
control point grid size m	257×257

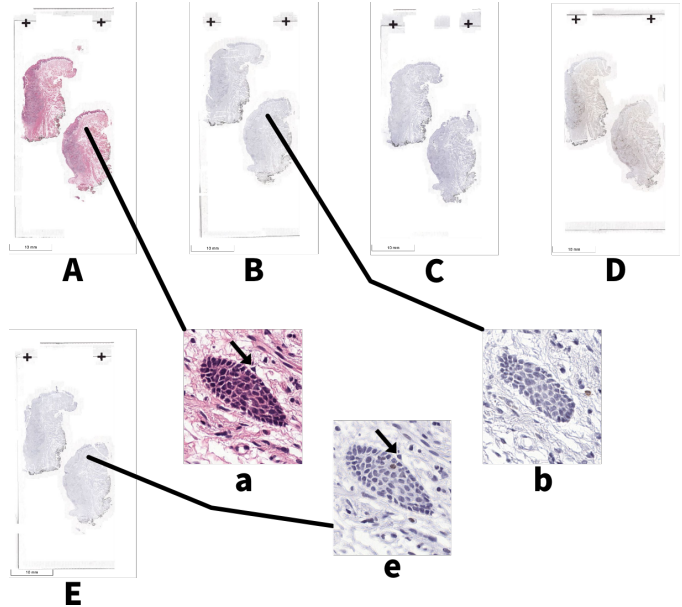


Fig. 3. One of nine sets of the HyReCo data. Slides A–D are consecutive stains (H&E, CD8, Ki67, CD45RO). Slide E is washed and re-stained from slide A. In the cropped images a, b, and e corresponding nuclei can be found only between the re-stained slide pair a and e.

further re-stained slides were annotated. For this, an additional number of 2303 annotations were produced for 54 additional image pairs of H&E-PHH3 (ca. 43 annotations per pair). These have again been verified by two experienced researchers.

We use this combined consecutive and re-stained dataset for a comparison of the registration accuracy of both techniques. We further compare parametric and non-parametric registration methods to evaluate the need for non-parametric registration in both cases.

The dataset including the landmarks has been made available at <https://doi.org/10.5281/zenodo.4056521> under the Creative Commons Attribution-ShareAlike 4.0 International license⁵ [14].

⁵<https://creativecommons.org/licenses/by-sa/4.0/>

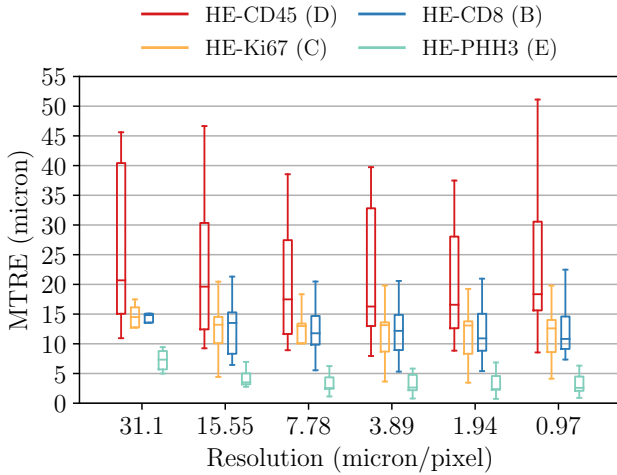


Fig. 4. MTRE after non-parametric registration at different image resolutions (HyReCo dataset). The MTRE between re-stained section (turquoise) is visibly lower than between consecutive sections.

1) Registration Accuracy: The resulting landmark errors after applying the 3-step registration to the HyReCo data are shown in Figure 4. Comparing different image resolutions, the MTRE shows no clear reduction beyond 7.78 $\mu\text{m}/\text{px}$. The MMTRE in re-stained images reaches 2.4 μm and is approximately five times lower than between consecutive sections (Table 2).

TABLE II

MINIMAL LANDMARK ERRORS REACHED FOR RE-STAINED AND CONSECUTIVE IMAGE PAIRS IN THE HYRECO DATASET AND THEIR REQUIRED IMAGE RESOLUTION. RE-STAINED LANDMARK ERRORS ARE APPROXIMATELY FIVE TIMES SMALLER THAN IN CONSECUTIVE SECTIONS AND REACH THE ORDER OF MAGNITUDE OF A CELL NUCLEUS.

pair of stains	min MMTRE	im. resolution
HE-PHH3 (re-stained)	2.4 μm	1.94 $\mu\text{m}/\text{px}$
HE-CD8 (consecutive)	10.8 μm	0.97 $\mu\text{m}/\text{px}$
HE-Ki67 (consecutive)	12.6 μm	0.97 $\mu\text{m}/\text{px}$
HE-CD45RO (consecutive)	16.3 μm	3.89 $\mu\text{m}/\text{px}$
mean consecutive	13.2 μm	

From the landmark errors of each staining we are also able to derive the likely section order (HE, CD8, Ki67, CD45RO). As the distance between two sections grows, the landmark error increases as well.

2) Accuracy of Non-Parametric Compared to Parametric Registration: Comparing non-parametric and parametric registration, consecutive sections show a clear advantage in non-parametric registration (Figure 5). If computed purely between re-stained sections, the non-parametric component of the deformation also lowers the landmark error (Figure 6), but to a lower degree than between consecutive sections. A good alignment of the two sections can be observed in most regions in a visual comparison (Figure 7).

3) Computation Times of Non-Parametric Compared to Parametric Registration: The computation times depend largely on the size of the input images. For parametric registration, the

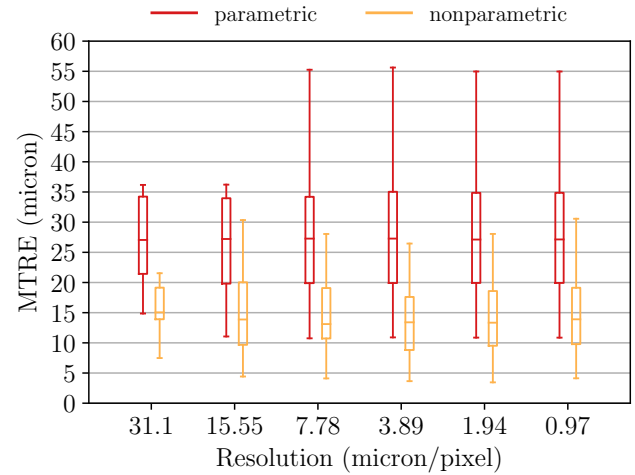


Fig. 5. Median TRE after parametric and non-parametric registration of consecutive image pairs at different image resolutions (HyReCo dataset). Non-parametric registration is always more accurate than parametric registration.

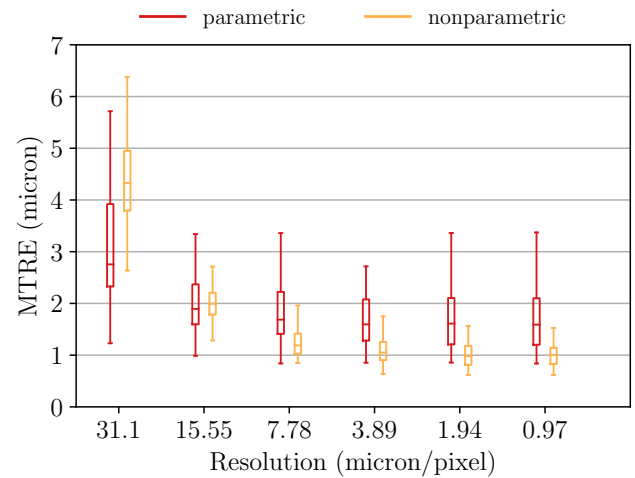


Fig. 6. Median TRE after parametric and non-parametric registration of re-stained image pairs at different image resolutions. Non-parametric registration does further improve the landmark error if compared to parametric registration.

average computation time ranges from 1 second (image size 780 x 1720, 31.1 $\mu\text{m}/\text{pixel}$) to 8 minutes (image size 25000 x 55000, 0.97 $\mu\text{m}/\text{pixel}$) on an Intel(R) Core(TM) i7-7700K CPU (4.20GHz, four cores) with 32 GB of RAM.

For non-parametric registration, the average computation time ranges from 4 seconds (image size 780 x 1720, 31.1 $\mu\text{m}/\text{pixel}$) to 20 minutes (image size 25000 x 55000, 0.97 $\mu\text{m}/\text{pixel}$) on an Intel(R) Core(TM) i7-7700K CPU (4.20GHz, four cores) with 32 GB of RAM.

IV. DISCUSSION

The average MTRE between consecutive sections is larger in the ANHIR dataset than in the HyReCo data. These can be explained by a higher level of structural differences in the

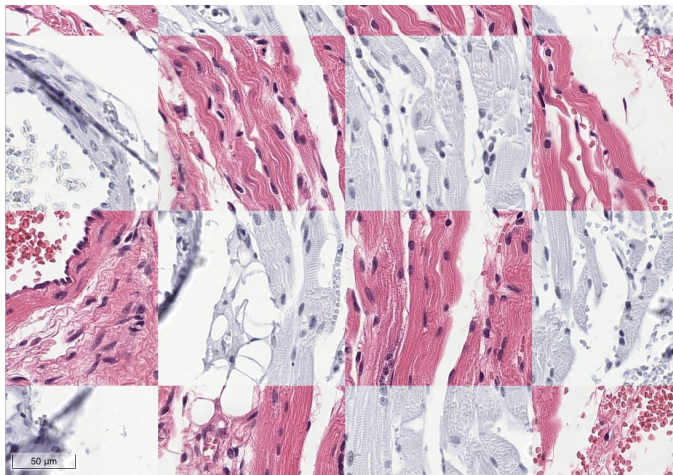


Fig. 7. Checkerboard plot after registration of a re-stained image pair. Nucleus correspondences are visible at the borders of the checkerboard tiles.

ANHIR images (see e.g. [5] Fig. S3) and a lower average image resolution where some cases have only a tenth of the resolution of the HyReCo data.

Registering re-stained sections allows for a higher accuracy. A MMTRE of $1.0 \mu\text{m}$ allows nucleus-level alignment which is infeasible in serial sections where the same nucleus is often not present on the next slide. For comparison, the size of an average mammalian nucleus is ca. $6 \mu\text{m}$ [1], while tissue sections are typically $3\text{--}5 \mu\text{m}$ thick. The increased accuracy comes at the price of the loss of the physical stained glass slide and an increased processing time due to the de-staining. Only the stain that is applied last can be conserved. Especially in clinical settings, long-term storage of the glass slides and short time to diagnosis are important.

Smaller nonlinear deformations occur in the re-staining process due to the mechanical and chemical manipulation. These nonlinear components can also be observed in the deformation fields resulting from the registration of re-stained images. When aiming at a high registration accuracy in re-stained images, non-parametric image registration further decreases the landmark error in fine image resolutions.

A. Conclusion

We compared the parametric and non-parametric registration of consecutive and re-stained sections of histological specimens. Registrations were evaluated in terms of landmark error, where landmarks have been placed prior to registration in all image pairs.

For cell-to-cell correspondence, re-stained images lead to a much more accurate alignment due to the vanishing differences in cellular structure between the two images. Also, in these cases, a parametric (affine) registration of high resolution images already leads to an accurate alignment up to a MMTRE of $1.6 \mu\text{m}$. Non-parametric registration further improves the registration result to a MMTRE of $1.0 \mu\text{m}$. As previously demonstrated [6, 24], the high accuracy of the alignment makes re-stained tissue sections a good source of ground truth data for deep-learning training.

For consecutive sections as they occur for example in 3D reconstruction, non-parametric registration also leads to the more accurate results. Here, the structural differences between the two sections are larger which increases the difference between parametric and non-parametric registration results.

In all cases, increasing the image resolution leads to higher registration accuracy. In re-stained sections, the required image resolution to reach the optimal landmark error is higher than in consecutive sections. Here registration accuracy might still be limited by the computer's memory which limits the image size that can be used for registration. In these cases, patch-based approaches [16] might be able to increase the registration accuracy beyond the results in this study.

REFERENCES

- [1] Bruce Alberts, ed. *Molecular biology of the cell*. 4th ed. New York: Garland Science, 2002. 1548 pp.
- [2] Grace Banik et al. "High-dimensional multiplexed immunohistochemical characterization of immune contexture in human cancers". In: *Methods in Enzymology*. Vol. 635. Elsevier, 2020, pp. 1–20. DOI: 10.1016/bs.mie.2019.05.039.
- [3] Millard F. Beatty. *Principles of Engineering Mechanics*. Mathematical Concepts and Methods in Science and Engineering 32–33. New York: Plenum Press, 1986.
- [4] Jiri Borovec, Arrate Munoz-Barrutia, and Jan Kybic. "Benchmarking of Image Registration Methods for Differently Stained Histological Slides". In: *2018 25th IEEE International Conference on Image Processing (ICIP)*. Athens: IEEE, 2018, pp. 3368–3372. DOI: 10.1109/ICIP.2018.8451040.
- [5] Jiri Borovec et al. "ANHIR: Automatic Non-Rigid Histological Image Registration Challenge". In: *IEEE Transactions on Medical Imaging* 39.10 (2020), pp. 3042–3052. DOI: 10.1109/TMI.2020.2986331.
- [6] Wouter Bulten et al. "Epithelium segmentation using deep learning in H&E-stained prostate specimens with immunohistochemistry as reference standard". In: *Scientific Reports* 9.1 (2019). DOI: 10.1038/s41598-018-37257-4.
- [7] Bernd Fischer and Jan Modersitzki. "Curvature Based Image Registration". In: *Journal of Mathematical Imaging and Vision* (2003), pp. 81–85.
- [8] Bernd Fischer and Jan Modersitzki. "Fast Image Registration - A Variational Approach". In: *Numerical Analysis and Computational Mathematics*. Ed. by G Psihogios. 2003, pp. 69–74.
- [9] M. J. Gerdes et al. "Highly multiplexed single-cell analysis of formalin-fixed, paraffin-embedded cancer tissue". In: *Proceedings of the National Academy of Sciences* 110.29 (2013), pp. 11982–11987. DOI: 10.1073/pnas.1300136110.
- [10] E. Haber and J. Modersitzki. "Intensity Gradient Based Registration and Fusion of Multi-Modal Images". In: *Methods of Information in Medicine* 46.03 (2007), pp. 292–299. DOI: 10.1160/ME9046.

- [11] Eldad Haber and Jan Modersitzki. “A Multilevel Method for Image Registration”. In: *SIAM Journal on Scientific Computing* 27.5 (2006), pp. 1594–1607.
- [12] Nathalie Harder et al. “Automatic discovery of image-based signatures for ipilimumab response prediction in malignant melanoma”. In: *Scientific Reports* 9.1 (2019), p. 7449. DOI: 10.1038/s41598-019-43525-8.
- [13] Lars König et al. “A Matrix-Free Approach to Parallel and Memory-Efficient Deformable Image Registration”. In: *SIAM Journal on Scientific Computing* 40.3 (2018), B858–B888. DOI: 10.1137/17M125522.
- [14] Jeroen van der Laak, Johannes Lotz, and Nick Weiss. *HyReCo - Hybrid re-stained and consecutive histological serial sections*. 2020. DOI: <https://doi.org/10.5281/zenodo.4056521>.
- [15] Jia-Ren Lin et al. “Highly multiplexed immunofluorescence imaging of human tissues and tumors using t-CyCIF and conventional optical microscopes”. In: *eLife* 7 (2018), e31657. DOI: 10.7554/eLife.31657.
- [16] Johannes Lotz. “Combined local and global image registration and its application to large-scale images in digital pathology”. PhD thesis. University of Lübeck, 2020. DOI: <http://d-nb.info/1217024069>.
- [17] Jan Modersitzki. *FAIR: Flexible Algorithms for Image Registration*. SIAM, 2009.
- [18] Sanjay Mukhopadhyay et al. “Whole Slide Imaging Versus Microscopy for Primary Diagnosis in Surgical Pathology: A Multicenter Blinded Randomized Noninferiority Study of 1992 Cases (Pivotal Study)”. In: *The American Journal of Surgical Pathology* (2017), p. 1. DOI: 10.1097/PAS.0000000000000948.
- [19] Jorge Nocedal and Stephen J Wright. *Numerical optimization*. New York: Springer, 2006.
- [20] Romain Remark et al. “In-depth tissue profiling using multiplexed immunohistochemical consecutive staining on single slide”. In: *Science Immunology* 1.1 (2016), aaf6925–aaf6925. DOI: 10.1126/scimmunol.aaf6925.
- [21] Jan Rühaak et al. “Highly Accurate Fast Lung CT Registration”. In: *Proceedings of SPIE* 8669, *Medical Imaging 2013: Image Processing* (2013).
- [22] Oliver Schmitt et al. “Image Registration of Sectioned Brains”. In: *International Journal of Computer Vision* 73.1 (2006), pp. 5–39. DOI: 10.1007/s11263-006-9780-x.
- [23] Guoli Song et al. “A Review on Medical Image Registration as an Optimization Problem”. In: *Current Medical Imaging Reviews* 13.3 (2017). DOI: 10.2174/1573405612666160920123955.
- [24] David Tellez et al. “Whole-Slide Mitosis Detection in H&E Breast Histology Using PHH3 as a Reference to Train Distilled Stain-Invariant Convolutional Networks”. In: *IEEE Transactions on Medical Imaging* 37.9 (2018), pp. 2126–2136. DOI: 10.1109/TMI.2018.2820199.